Study of Bubbling and Slugging Fluidized Beds by Simulation and ECT

Haigang Wang and Wuqiang Yang
School of Electrical and Electronic Engineering, The University of Manchester, P.O. Box 88, Manchester M60 1QD, U.K.

Tom Dyakowski
School of Chemical Engineering and Analytical Science, The University of Manchester, P.O. Box 88, Manchester M60 1QD, U.K.

Shi Liu
Institute of Engineering Thermophysics, Chinese Academy of Sciences, P.O. Box 2706, Beijing 100080, China

DOI 10.1002/aic.10904
Published online July 5, 2006 in Wiley InterScience (www.interscience.wiley.com).

Fluidization conditions in a circulating-fluidized bed (CFB) can vary dramatically, from bubbling to circulating regimes. The granular Eurlerian models have been used to simulate the bubbling and slugging behavior of gas and solids in CFB. Considering the dielectric properties and rapid movement of solids in CFB, electrical capacitance tomography (ECT) is particularly suitable for measuring the concentration and distribution of solids in CFB to verify the simulation results. The simulation results by computational fluid dynamics (CFD) analysis and experimental results obtained by ECT are reported, and compares the simulation and experimental results first time, including the solids concentration profile, temporal variation of average-solids concentration, autocorrelation coefficient and frequency spectrum.
 AIChE J, 52: 3078–3087, 2006
Keywords: circulating fluidized bed, multiphase flow, CFD, electrical capacitance tomography

Introduction

Fluidized beds are commonly used in chemical, petroleum, process and power industries, for example, for drying, catalytic reaction and coal combustion. In particular, circulating-fluidized beds (CFB) have been extensively studied for efficient and clean coal combustion in the next generation of power plants.

The efficiency of heat and mass transfer in a fluidized bed is a function of operational parameters, such as the gas flow rate, particle size, particle density and height of settled bed. Also, it strongly depends on the gas-solids flow pattern. It is well known that the dynamics of a fluidized bed can be characterised by two time-scales. Large-scale fluctuation occurs owing to formation of bubbles during fluidization, and arising from the circulating motion of particles. Small fluctuation is induced by the interphase interaction between individual particles or collections of particles. In particular, the flow pattern just above the air distributor at the bottom of a fluidized bed is determined by gas-particle interaction, particle-particle interaction and bubble coalescence. Therefore, these interactions in the time domain can be characterized by both large and small fluctuations. A qualitative and quantitative description of the gas-solids hydrodynamics just above the air distributor is fundamental for understanding the mechanism responsible for transition between bubbling and slugging-flow regimes, and is critical to ascertain the optimum design of a fluidized-bed system, which should be characterized by a high-efficiency of heat and mass transfer between gas and solids phases. How-

Correspondence concerning this article should be addressed to H. G. Wang at Haigang.Wang@manchester.ac.uk.

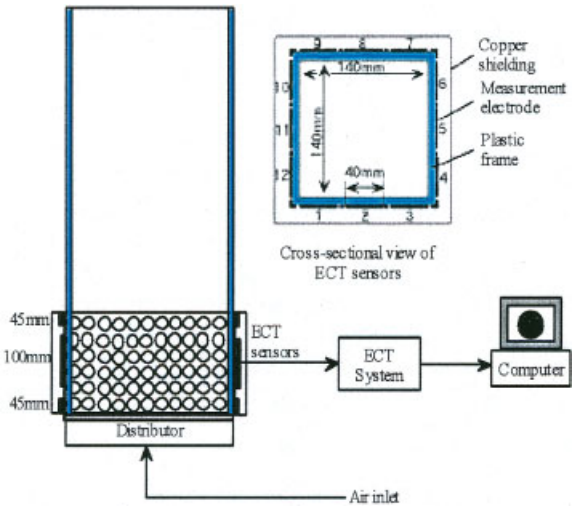

Figure 1. Experiment setup and ECT sensor.

[Color figure can be viewed in the online issue, which is available at www.interscience.wiley.com.]

ever, it is very difficult to investigate this fluidization phenomenon using radiation-based methods because of the rapid fluctuation (over intervals of milliseconds or less) of voidage in a fluidized bed.

The continuing development of electrical capacitance tomography (ECT) provides an opportunity to investigate the fluidization phenomena. ECT is particularly suitable for two-phase gas-solids systems, and has been used to investigate pneumatic conveyors and fluidized beds. A number of researchers[1,2,3,4,5] have investigated the internal structures of bubbling-fluidized beds, and have shown the movement of bubbles. As an example, an ECT system was used to investigate the growth of bubbles near the bottom of a bubbling-fluidized bed.[4] Liu et al.[6] compared the solids concentration in a fluidized bed measured by ECT, with the data measured by a pressure difference method, showing a good agreement under high-concentration conditions. Du et al.[7] also investigated the internal structures in fluidised beds of various diameters, and demonstrated the capability of ECT for small beds with a diameter up to 0.3 m.

Usually, circular ECT sensors are used for applications in the process industry. Since square or rectangular CFB are commonly used in some other industries, such as the power industry for coal combustion, there is a demand on ECT to image such apparatus. For this purpose, a square sensor has been developed.[8] Prior to the study reported by this article, some preliminary results have been reported on real-time measurement of square fluidized beds.[9,10]

Table 1. Experiment Conditions

Experiment Unit	Operating Condition
Column	Cross section: 140 × 140 mm Height: 2.8 m Material: sand
Distributor	Perforated PVC: 81 holes of 6 mm in diameter
Fluidizing gas	Air at ambient condition
ECT system	Single plane, 12 electrodes, AC-based ECT[17]
Experimental span	110 seconds

Table 2. Physical Properties of Particles

Particle	Size or Dimension
Mean particle diameter	0.3 mm
Particle density	2660 kg/m^3
Height of static bed	200 mm

With ECT, a two-phase system is interrogated by an array of sensing electrodes from many different viewing angles around a cross-section. Capacitance between each pair of electrodes is measured. With the sensing area being divided into many virtual pixels (typically 32 × 32), an image representing the cross-sectional distribution of materials is reconstructed, using the measured capacitance data and certain image reconstruction algorithms. In this research, an optimized iterative method based on the Landweber method is used for reconstructing images.[10,11]

In this article, simulation results obtained by computational-flow dynamics (CFD) analysis using software package FLUENT and experimental results obtained by ECT are reported. Two-fluidization regimes, namely bubbling and slugging, are investigated. Solids fluctuation is analyzed using the time series theory, such as the fast-Fourier transform (FFT) and autocorrelation. Some statistical parameters, such as the frequency spectrum of time series of solids concentration, autocorrelation coefficient, probability-density function (PDF) of solids concentration, and nonlinearity are analyzed for understanding the chaotic behaviour of solids in CFB.

Description of Physical and Numerical Model

Governing equations

The two-fluid models[12,13] are the most commonly used for the simulation of fluidized beds, in which the fluid phase and the particulate phase are assumed to behave like two interpenetrating continua. The conservation equations employed in the models can be seen as a generalization of the Navier-Stokes equations for interacting continua. In this research, the gas-solids two-phase flows in CFB are three-dimensional (3-D), nonsteady and without heat and mass transfer. The governing equations in

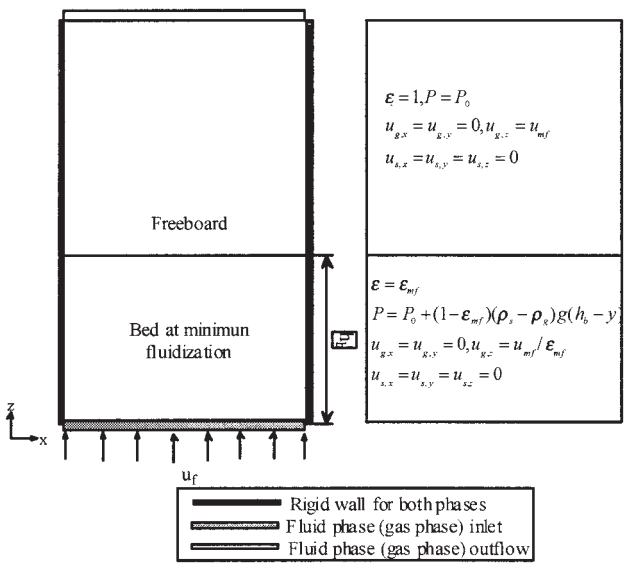

Figure 2. Boundary and initial conditions of CFD.

Table 3. Model Parameters for CFD

Parameter	Value	Comment or Reference
Particle diameter (d_s)	0.3 mm	No size distribution
Particle density (ρ_s)	2660 kg/m^3	Sands
Coefficient of restitution (e) (Particle-particle interaction)	0.9	Pain et al.[22]
Coefficient of restitution (e) (Particle-wall interaction)	0.75	Pain et al.[22]
Maximum-solids fraction ($\varepsilon_{s,\max}$)	0.61	Wachem et al.[23]
Minimum-fluidization velocity (u_{mf})	0.09 m/s	From Ergun[24]
Time-step (Δt)	0.2 ms	For convergence
Settled-bed height (h)	200 mm	Fixed value
Column height (H)	1.0 m	Fixed value
Mesh spacing ($\Delta x \times \Delta y \times \Delta z$)	0.5 × 0.5 × 0.5 cm	To reduce numerical diffusion

the Cartesian (x, y, z) coordinate system for the conservation of mass and momentum for each phase are given by

$$\frac{\partial \varepsilon_g \rho_g}{\partial t} + \nabla \cdot (\varepsilon_g \rho_g \vec{V}_g) = 0 \quad (1)$$

$$\frac{\partial \varepsilon_s \rho_s}{\partial t} + \nabla \cdot (\varepsilon_s \rho_s \vec{V}_s) = 0 \quad (2)$$

$$\frac{\partial}{\partial t}(\varepsilon_g \rho_g \vec{V}_g) + \nabla \cdot (\varepsilon_g \rho_g \vec{V}_g \vec{V}_g) = -\varepsilon_g \nabla p + \nabla \cdot \bar{\bar{\tau}}_g + \varepsilon_g \rho_g g - \beta(\vec{V}_g - \vec{V}_s) \quad (3)$$

$$\frac{\partial}{\partial t}(\varepsilon_s \rho_s \vec{V}_s) + \nabla \cdot (\varepsilon_s \rho_s \vec{V}_s \vec{V}_s) = -\nabla p_s - \varepsilon_s \nabla p + \nabla \cdot \bar{\bar{\tau}}_s + \varepsilon_s \rho_s g - \beta(\vec{V}_s - \vec{V}_g) \quad (4)$$

The above mass and momentum conservation equations contain unknown velocities and instantaneous void fractions ε_g and ε_s. An additional algebraic equation based on volume continuity is

$$\varepsilon_g + \varepsilon_s = 1 \quad (5)$$

Kinetic theory of granular flow

This model requires additional constitutive equations to describe the gas and solids stress tensors $\bar{\bar{\tau}}_g$ and $\bar{\tau}_s$, gas-particle interphase drag coefficient β and solids pressure p_s. Ding and Gidaspow,[14] Gidaspow et al.[13,15] and Lun et al.[16] reported the use of the kinetic theory for modelling granular flows. Non-ideal (that is, no elastic) particle-particle collisions are modeled using the concept of granular temperature, which is defined by

$$\theta = \tfrac{1}{3}\langle \overline{C_p} \cdot \overline{C_p} \rangle \quad (6)$$

where $\overline{C_p}$ is a random fluctuating velocity of particles, and the brackets denote ensemble averaging.

The variation of the particle-velocity fluctuations is described by a separation equation, the so-called granular temperature equation.

$$\frac{3}{2}\left[\frac{\partial}{\partial t}(\varepsilon_s \rho_s \theta) + \nabla \cdot (\varepsilon_s \rho_s \theta \vec{V}_s)\right] = (-P_s I + \bar{\bar{\tau}}_s) : \nabla \vec{V}_s + \nabla \cdot (k_s \nabla \theta) - \gamma_s + \phi_s \quad (7)$$

The lefthand side of Eq. 7 is the net change of the fluctuating energy. It is equal to the sum of the generation of fluctuating energy $(-P_s I + \bar{\bar{\tau}}_s) : \nabla \vec{V}_s$, the diffusion of fluctuating energy

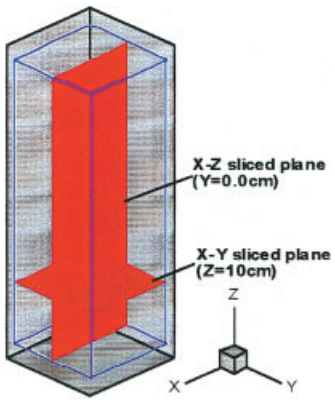

Figure 3. Sliced plane for analysis of CFD results.

[Color figure can be viewed in the online issue, which is available at www.interscience.wiley.com.]

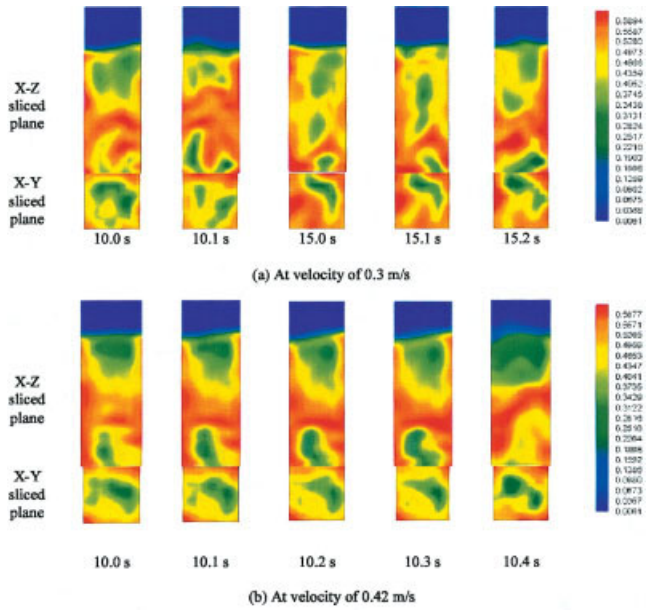

Figure 4. Instantaneous particle-concentration distributions.

[Color figure can be viewed in the online issue, which is available at www.interscience.wiley.com.]

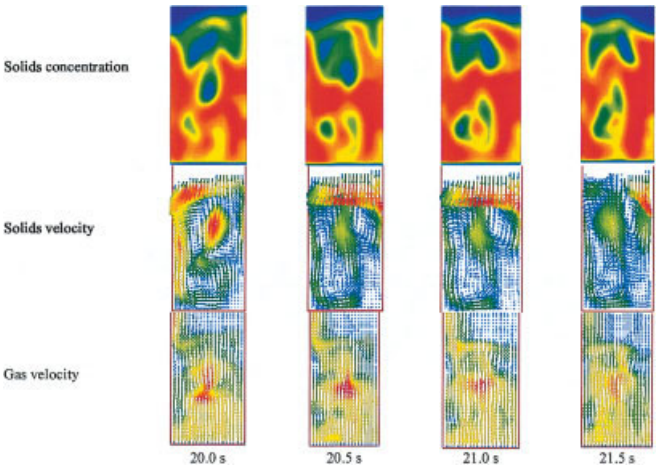

Figure 5. Instantaneous particle concentration, particle velocity and gas velocity in bubbling fluidization.

[Color figure can be viewed in the online issue, which is available at www.interscience.wiley.com.]

$\nabla \cdot (k_s \nabla \theta)$, the dissipation γ_s, and the exchange of granular temperature between the gas and solids phase ϕ_s.

In FLUENT, there are four methods to solve the solids granular temperature: (1) algebraic formulation, (2) partial-differential equations, (3) constant granular temperature, and (4) user define function. In the following simulation, partial-differential equations are used to solve the granular temperature.

Constitutive equations

The interphase momentum transfer is an important term in the modelling of gas-particle interactions, since fluidization of particles results from the drag exerted by interstitial gas on the particulate phase. The form and skin drag are combined in one semiempirical parameter, the interphase momentum-transfer coefficient β, which is given by Eqs. (A1–A4) in the Appendix. The Newtonian viscous stress of the gas phase and stress tensor of the solids phase is given by Eqs. A5–A6. Results from the kinetic theory model for granular phase constitute relations that are given by Eqs. A7–A13, in which the pressure of the solids phase described by Eq. A9, and viscosities described by Eq. A10, are dependent on the granular temperature θ as described by Eq. 7.

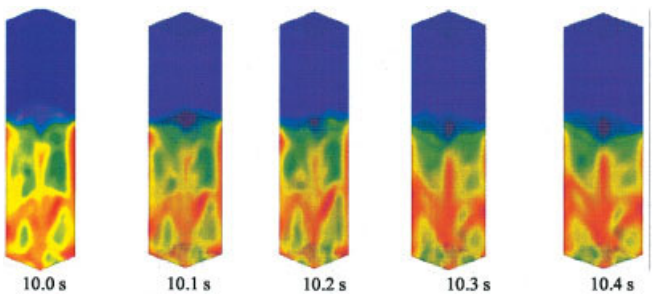

Figure 6. Bubbling behaviour in 3-D.

[Color figure can be viewed in the online issue, which is available at www.interscience.wiley.com.]

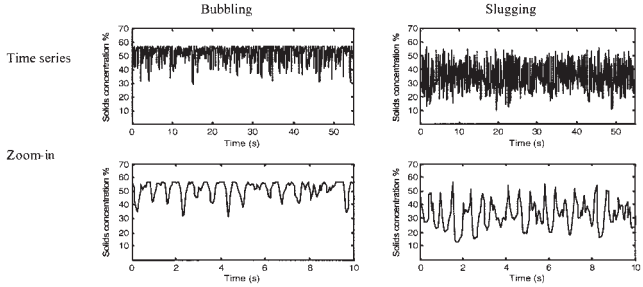

Figure 7. Average solids concentration.

Experiment setup

A CFB setup with an ECT sensor for tests is shown in Figure 1. The detailed parameters, such as the experimental conditions and physical properties of particles, are listed in Tables 1 and 2. The superficial fluidization velocity u_{mf} was chosen to cover a range of conditions, from bubbling to slugging regimes, with a minimum velocity of 0.04 m/s, and a maximum velocity of 1.5 m/s. Twelve electrodes are mounted on the outside wall of the fluidized bed, with three electrodes on each side. The electrodes are enclosed to eliminate external interference. Each electrode has a length of 10 cm and width 4 cm. The measurement region encompasses a height between 5 and 15 cm above the air distributor for the measurement plane. Therefore, each pixel in the ECT image represents an axial average over this rectangle measurement volume.

Simulation and experimental results and data analysis

Eqs. 1–7 with the boundary and initial conditions as shown in Figure 2 were solved numerically using FLUENT, which uses a control-volume-based technique to convert the governing Eqs. (1–7) to algebraic equations on each finite cell so that they can be solved numerically. With the control-volume technique, the governing equations about each control-volume are integrated and discrete equations are obtained. This conserves each quantity on a control-volume basis to avoid attendant numerical issues including interpolation functions. The number of equations and unknown parameters are listed in the Appendix Table A1. There are 20 equations and the same number of unknown parameters. The wall of CFB is treated as nonslip boundary for the gas phase, that is, the velocity of the gas phase is set to zero at the wall. For the solids phase, the free slip condition is assumed, that is, there is no hindrance in the downward or upward velocity of the particles when they are near the wall. The granular temperature of the solids phase at the wall was given in a reference.[18] At the outlet, the ambient

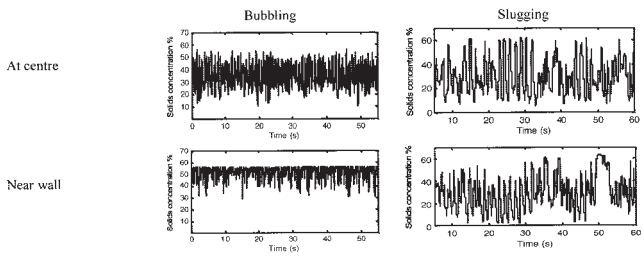

Figure 8. Solids concentration at single point.

Table 4. Variation of Solids Concentration at Single Point by CFD Simulation

Flow Regime	Bubbling		Slugging	
Point Position	Center	Near Wall	Center	Near Wall
Min of λ (%)	1.68	1.06	0.573	0.25
Max of λ (%)	60.8	60.7	60.7	60.5
Mean of λ (%)	29.6	50.6	39.3	54.4
SD	0.149	0.106	0.189	0.106

Table 5. Variation of Solids Concentration at Single Point from ECT Results

Flow Regime	Bubbling		Slugging	
Point Position	Center	Near Wall	Center	Near Wall
Min of λ (%)	1.68	3.06	1.17	0.15
Max of λ (%)	66.8	67.3	62.0	65.9
Mean of λ (%)	51.3	55.7	31.1	45.2
SD	0.127	0.176	0.134	0.106

atmosphere pressure and continuous mass fluxes of both gas and solids are assumed. Initially the bed is operated at incipient fluidization conditions, with a superficial gas velocity above the minimum fluidization velocity. More details on the solids-phase boundary are given by Sinclair and Jackson.[19] It has been shown[20,21] that under the same conditions there is significant difference between the 2-D and 3-D simulation. In fact, 2-D simulation can only be used for sensitivity analysis, and quantitative validation must be done in 3-D. Therefore, a fully 3-D CFB model was assumed for the simulation. A uniform finite element cell of 28 × 28 × 200 in the x, y and z directions, respectively, was used. It has been shown that 100 cm height domain for the simulation is adequate to minimize the effect of the imposed outlet boundary conditions on the main flow. Simulations were performed for 115 s with a time-step size of 0.2 ms. The simulation parameters are listed in Table 3. The height of CFB column is 1.0 m, and the average gas velocity lies between 0.2 and 0.5 m/s as listed in Table 1. The fluidized gas takes about 5 s to pass through the channel of the bed. To disregard the effect of the impulsive initialisation effect, the first 5 s were neglected. To validate the CFD results, images were reconstructed using ECT with a square grid, 28 × 28 pixels. The size of each pixel is 0.5 × 0.5 cm, which is the same as the CFD simulation. The imaging speed is 140 frames per second.

Solids concentration profile by CFD

Figure 4 shows the computed instantaneous particle concentration in the x–z and x–y sliced planes (as defined in Figure 3) at difference time. The fluidization velocity is 0.3 m/s in Figure 4a and 0.42 m/s in Figure 4b. As can be seen, bubbles were created near the bottom corners of the bed at t = 10.0 s, and then moved up and grown at time t = 10.1 s, which is clearly shown in the x–y cross section. At t = 15.0 s, another bubble was created and moved up. Also, at t = 15.0 s, two bubbles coalesced can be seen at the top of Figure 4a. This coalescence behavior is consistent with the explanation by Clift and Grate.[25] As a result of coalescence near the top of the bed, bubbles in this region are larger than those near the bottom. Since at the top of the bed the size of the bubble is comparable with the diameter of the bed, the fluidized bed is mainly working in the slugging regime. These phenomena are clearly shown in Figure 4b.

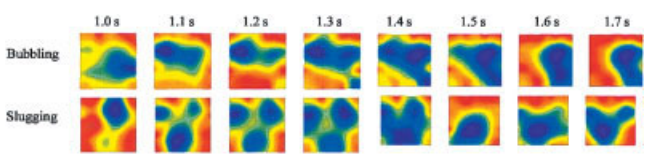

Figure 9. Cross-sectional concentration of solids.

[Color figure can be viewed in the online issue, which is available at www.interscience.wiley.com.]

Clift and Grace[25] explained that, as a bubble approaches the upper free surface of a fluidised bed, a dome was seen to rise in advance of the bubble. A mantle of solids separating the top of the dome from the roof of the bubble diminished in thickness, until the bubble broke through. Similar behavior can be observed in the volume-concentration distribution of particles in Figure 4. Periodically, relatively large bubbles burst through the bed surface, collapse rapidly and then new bubbles slowly re-expand the bed.

Bubbles are subject to elongation when rising along vertical tubes,[26] or during interaction with the wall or other bubbles. It has been shown by the simulation that other bubbles play an important role in the elongation of bubbles. Figure 5 shows the elongation of a bubble along the central axis of the bed. The effect of other bubbles on the change in direction, shape and velocity of the bubble are clearly seen in Figure 4. Three counter-rotating vortices created along the bubble, at time t = 20.0 s, can be seen in the particle velocity vectors. At time t = 21.5 s the fourth vortex is created near the bottom of the bed. It can also be seen from the gas velocity vectors of the gas phase that the gas enters from the bottom of the bubble and exits at the top. Figure 6 shows the bubble in the bed in 3-D, indicating the effect of the wall on the elongation of the bubble.

Figure 7 shows the time series of average solids concentration λ along a cross-sectional profile, which is axial average between z = 5 cm and z = 15 cm above the bottom of the distribution plate. A zoomed portion of each curve is shown in the bottom of each figure. In the bubbling fluidization regime, λ varies from 21.8% to 60.9%, with a mean λ of 52.3%. In slugging fluidization regime, the fluctuation is much larger than in the bubbling regimes and λ varies from 18.0% to 58.9%, with a mean value of 33.0%. In Figure 8, the behavior of solids at different positions in the fluidized bed is compared. The point near the wall has a more complex fluctuation than that in the centre. Table 4 lists the details of the variation of λ for different flows.

Solids concentration profile measurement by ECT

As mentioned earlier, ECT images were reconstructed with a square grid, 28 × 28 pixels. The size of each pixel is 0.5 × 0.5 cm which is the same as the CFD. Two sequences of images for bubbling and slugging fluidization are shown in Figure 9.

The solids concentration shown in these images varies between 28% and 59% in the bubbling bed with an average of 52.1%, and varies between 13% and 58% in the slugging bed with an average of 36%. Table 5 lists the details of the variation of λ at the same points as in Table 4 for bubbling and slugging regimes. It can be seen that there is a region of low-solids

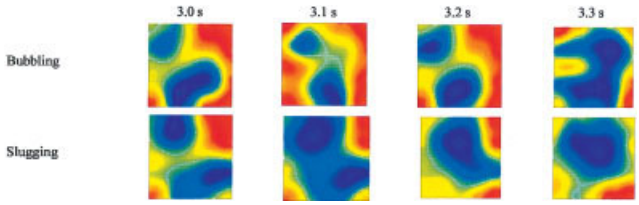

Figure 10. Elongation process of two bubbles.

[Color figure can be viewed in the online issue, which is available at www.interscience.wiley.com.]

concentration, close to the center of CFB, showing the character of the bubbling and slugging regimes. From the experimental results, it can be concluded that the cross-sectional area is largely occupied by solids with scattered gas bubbles in bubbling and slugging regimes. In the slugging regime, the concentration profile varies dramatically with the alternating appearance of large bubbles, sometimes with a single bubble and sometimes with two or more bubbles. The average concentration is also smaller than in the bubbling regime. From the earlier features, the flow regimes of the CFB can be easily identified.

From the ECT results, interaction between bubbles can be seen, which present similar behavior to that obtained by the CFD simulation. In Figure 9, we can see the effect of the wall on the bubble elongation and other bubbles. At $t = 1.1$ s, there are three bubbles in the cross-section of the slugging bed, and then become one bubbles because of the bubble elongation at $t = 1.4$ s. At $t = 1.5$ s, there is only one big bubble. Figure 10 shows the elongation process of two bubbles in the bubbling and slugging bed. These phenomena are similar to the CFD results.

Bubble size in bubbling regime

Experimental work was carried out in the 1970's and 1980's to investigate the bubble behavior in gas-solids fluidised beds. Darton et al.[27] suggested a semiempirical model describing the bubble growth

$$D_b = 0.54(U_0 - U_{mf})^{0.4}(h + 4\sqrt{A_0})^{0.8}/g^{0.2} \qquad (8)$$

where D_b is the bubble diameter, h is the height of the bubble above the distributor, A_0 is the catchments area, which characterizes the distributor, and 0.54 is the experimental constant.

Darton et al.[27] defined a bubble as an area, where the solids concentration is below a certain value. Wachem et al.[23] chose

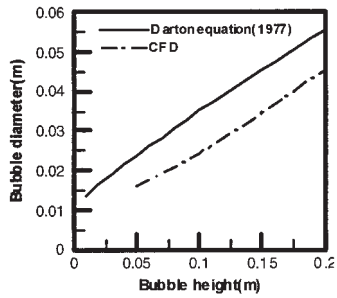

Figure 11. Bubble diameter vs. bed height in bubbling regime.

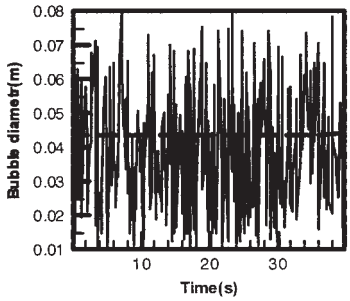

Figure 12. Variation in bubble diameter in bubbling regime obtained by ECT at the height of 0.15 cm above the air distributor.

this value to be 20%. Figure 11 shows the bubble diameter as defined by Darton et al. and the CFD results in the bubbling regime. It can be seen that the bubble diameter predicted by CFD are slightly smaller than that obtained by Eq. 8 in the bubbling regime. A possible reason for this is a deficiency of the measuring technique by Darton[27] in measuring very small bubbles. The condition and model for CFD simulation also influence the distribution of bubble diameters. In ECT measurement, one plane ECT sensor was used. Therefore, the bubble size is given in Figure 12 in one position only, at a height of 15 cm above the air distributor. The bubble diameter varies from 1 to 8 cm with a mean value of 4.35 cm, which is higher than that predicted by CFD, but close to the Darton's results. A possible reason is the point-spread effect of soft-field image reconstruction. This situation may be improved by applying a suitable threshold to the obtained images.

FFT is a commonly used technique for fluidisation analysis. In the past it has been employed extensively with pressure measurement to analyse the dynamic behavior and bubble frequency of fluidized beds.[28,29,30] In this work, this technique has been used for analyzing the fluctuation of the solids concentration, aiming to compare the CFD with ECT results.

Figure 13 shows the variation of the average solids concentration λ over the cross-section with time by ECT. The bubbling and slugging regimes present both different amplitude and different time behavior. In the bubbling regime, λ varies from 23.5% to 60%, with a mean λ of 52%. In the slugging regime, the fluctuation is much larger than in the bubbling and circulating regimes, and λ varies from 0.05% to 60% with a mean λ of 46.5%. The probability density function (pdf) for each flow regime was computed and shown in Figure 14 for both CFD and ECT results. In the bubbling regime, the difference between the two methods is very small, whereas in the slugging regime the difference is increased. Because of the fluctuation in the slugging regime, the particle behavior is more complex than that in the bubbling regime.

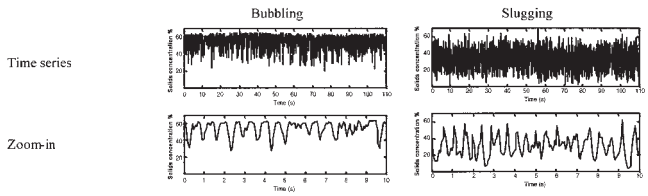

Figure 13. Average concentration.

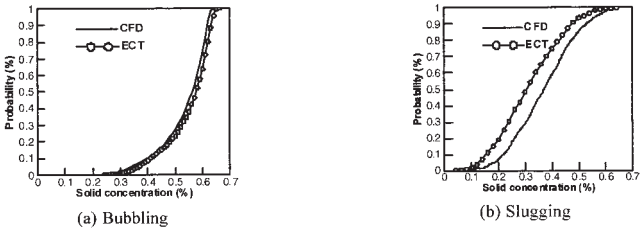

Figure 14. Probability vs. solids concentration.

To quantify the temporal patterns, autocorrelation functions were calculated for both the ECT and CFD results. Autocorrelation function between two points separated by a time lag, k time's Δt, is expressed as[31]

$$c_{xx} = \sum_{n=0}^{N-|k-1|} (\lambda(n) - \bar{\lambda})(\lambda(n-k) - \bar{\lambda}) \tag{9}$$

The autocorrelation function may be normalized by the value at zero lag, $c_{xx}(0)$, thus

$$c_{xx}(k) = \frac{c_{xx}(k)}{c_{xx}(0)} \tag{10}$$

where, $-1 \leq c_{xx} \leq 1$.

In Eq. 9

$$\bar{\lambda} = \frac{1}{N} \sum_{n=1}^{N} \lambda(n) \tag{11}$$

Figure 15 presents the autocorrelation functions. It can be seen that the decay in autocorrelation with time-lag is fast for the bubbling and slugging regimes. In the bubbling regime, it has a more periodic autocorrelation on a scale, which is similar to the bubble frequency. This seems to be a correlation with respect to the bubble dynamics.

It was reported that the pressure fluctuations in the bottom of the bed occurs between 0.5 and 1.4 Hz.[10,28] For comparison purposes, FFT is performed to obtain the frequency spectra of λ, and the results are shown in Figure 16. The frequency spectrum obtained by FFT clearly illustrates a peak corresponding to a frequency of about 1.4 Hz for the bubbling regime, and 1.2 to 2.0 Hz for the slugging regime according to both the CFD and ECT data. The finer structures in the frequency spectrum are shown in Figure 17. To study the fall-off

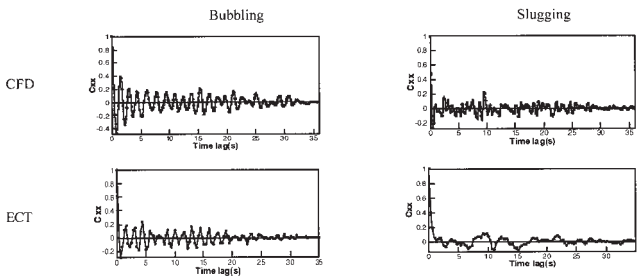

Figure 15. Autocorrelation coefficient.

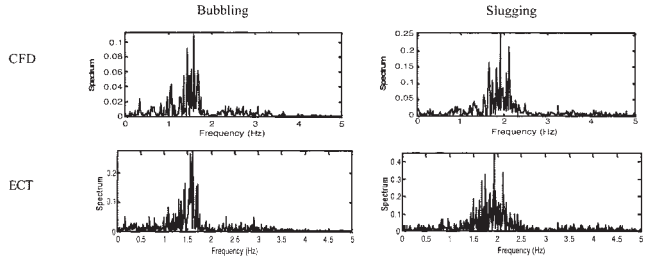

Figure 16. Frequency spectrum.

with frequency, the spectra are plotted on a logarithmic vertical axis vs. frequency. In spite of the large difference between the bubbling regimes, there is little difference between the power spectra above 1.5–10 Hz, as shown by the low-frequency macrostructure of the flow. It seems that 1.5–10 Hz is a transition range in the cases studied. The curves showed in Figure 17 can be divided into two regions: Region 1 (to the left of the vertical line), and Region 2 (to the right of the vertical line) from 2.5 to 10 Hz, which can be fitted as power-law ($Pxx \sim f^{\alpha}$) with about equal accuracy, around 2. The dominant frequencies reveal that they vary with the position in the bed, from 1 to 6 Hz.

In Figure 18 the dominant frequencies at the centre and near the wall in the bubbling and slugging regimes are compared. Table 6 summarizes the dominant frequency for the CFD and ECT results of two points. In the bubbling regime, CFD gives one dominant frequency about 1.8 Hz for the central point, and three frequencies 0.4, 0.9 and 1.6 Hz for the near wall point. ECT gives 0.4 and 1.5 Hz for the central point. In the near wall points the ECT results are 0.6, 1.5 and 2.7 Hz. In the snuggling regime, CFD and ECT give similar results. From these results, it can be seen that both CFD and ECT can reflect the complex solids behavior near the wall.

Time-average behavior for particles

Figure 19 shows the changes in the distribution of solids concentration along the height of a fluidized bed. The data from ECT were obtained at 10 cm above the air distributor. Numerical results were simulated at four difference positions as depicted.

For both bubbling and slugging regimes the results show significant evolution of solids concentration along the bed height. In particular, for a slugging regime a "crown-like" concentration can be observed, which is congruent with the

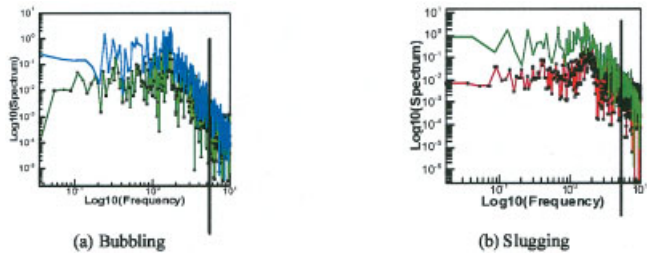

Figure 17. Power spectra (Line with square symbols—ECT results).

[Color figure can be viewed in the online issue, which is available at www.interscience.wiley.com.]

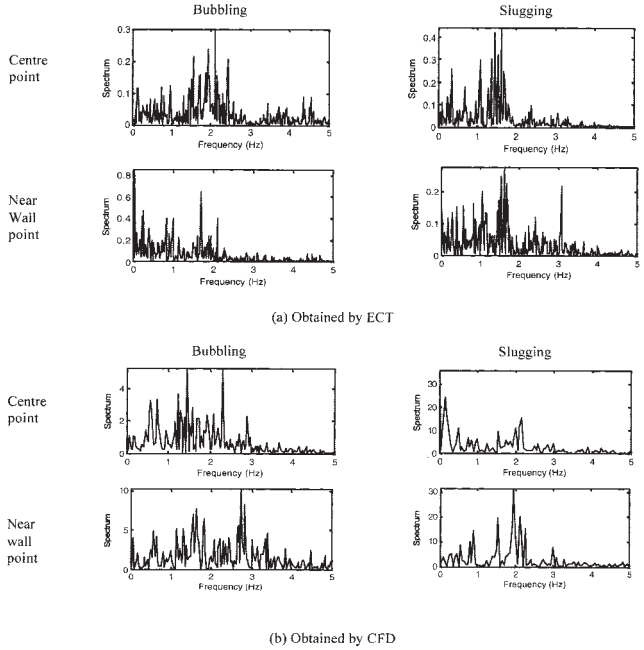

Figure 18. Average concentration and frequency spectrum.

results reported by Pain et al.[22,32] and Malcus et al.[33] Comparison between the measured and calculated values is given at the height of 10 cm above the air distributor. For a bubbling regime as shown in Figure 19a there is a good agreement between the calculated and measured values. For a slugging regime in the near wall region, the CFD results and ECT data also show a good agreement. However, in the central part of the channel there is nearly 100% difference between the measured and calculated values. It was reported that the accuracy of the ECT system decreases when the solids concentration is decreasing.[1]

In terms of cross-sectional average concentration, the data from ECT for a bubbling-flow regime are very close to those predicted by CFD simulations. For a slugging regime the difference between the cross-sectional average values is larger. As discussed earlier, it may be caused by errors in measuring lower-solids concentration in the central part of the bed.

The calculated solids velocity values, for the same positions as solids concentration, are presented in Figure 19c and d. For the both flow regimes the velocity profiles are developing from a relatively flat profiles at the lowest position above the air distributor ($h = 5$ cm) to a parabolic shape in the central part of the channel. Close to the wall the solids velocities are negative, which illustrates downward slides motion in this region. For the bubbling and slugging flow regimes, the difference between the maximum and the minimum velocities is 0.6 and 1.0 m/s respectively.

Table 6. Comparison of CFD and ECT Results in Terms of Dominant Frequency

	Bubbling		Slugging	
	CFD	ECT	CFD	ECT
Mean average	1.65	1.52	1.92	1.97
Center	1.8	0.4, 1.5	0.1, 2.1	1.6
Near wall	0.4, 0.9, 1.6	0.6, 1.5, 2.7	1.94	1.8

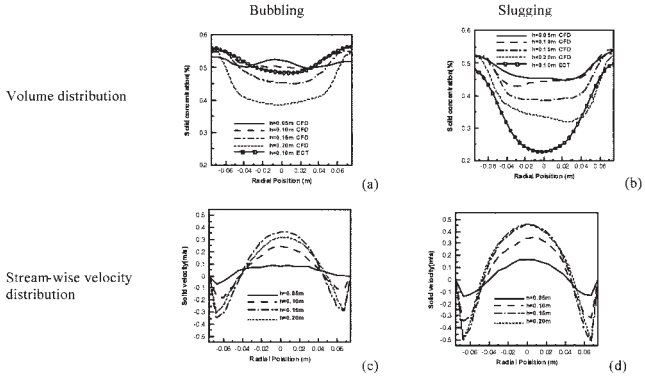

Figure 19. Time-average of particle distribution at different height of CFB.

Conclusions

This article presents a validation of CFD modelling of bubbling and slugging-flow regimes against the experimental data obtained from ECT. The presented CFD model consists of a set of mass and momentum conservation equations. The needed constitutive equations describing solids-solids interactions are derived from the granular theory. An ECT system was used for imaging the solids distribution instantaneously, with an imaging speed of 140 frames per second, within a square cross-sectional area. An optimized iterative algorithm based on the Landweber's method was applied for online imaging of the distribution of dielectric permittivity. The CFD results matched well with the ECT results. From these results, the following can be concluded:

(1) In the bubbling regime, the cross-section is largely occupied by solids with scattered gas bubbles. The instantaneous solids concentration averaged in a cross-sectional area varies from 23.5% to 60.0% with a mean average of 52.0%, which is close to 52.31% predicted by CFD. The ECT data show that the solids concentrations fluctuate more intensively near the wall than in the central area. The standard deviation of solids concentration is 0.176 in the near wall region and 0.127 in the central area. The dominant frequency lies between 0.8 to 2.1 Hz, and the mean bubble diameter is 4.35 cm by ECT. The calculated solids velocity profile has a flat character, and the values vary from -0.3 m/s close to the wall, and 0.4 m/s in the central area of the channel by CFD.

(2) In the slugging regime, the concentration profile varies dramatically with the alternating appearance of bubbles and dense solids. The average concentration of solids is 38.0% by CFD and 46.5% by ECT. On the other hand, the dominant frequency by the both methods is very close, which is lies between 1.2 and 2.0 Hz for both CFD and ECT.

(3) Both CFD and ECT can give detailed profile information describing the interaction between bubbles and between bubbles and the wall.

Due to the chaotic behavior of gas-solids distribution in CFB, further work is needed, such as using the chaotic theory to analyze the particle behavior by means of correlation dimension and Kolmogorov entropy through reconstructing the system attractor[34] in phase-space, and to calculate the chaotic invariants. Further improvement in image reconstruction for ECT would provide more reliable solids-distribution profile measurement.

Acknowledgments

The authors would like to thank EPSRC (GR/T29383/01), NSFC (50276062, 60532020) and British Council (PEK/0992/311) for sponsoring the research. Philip Ronson of the Sensing, Imaging and Signal Processing Group at the University of Manchester is thanked for his help in English.

Notation

A_0 = catchments area
C_d = drag coefficient
C_{xx} = auto-correlation coefficient
d_p = mean particle diameter, mm
D_b = bubble diameter, cm
e = particle-restriction coefficient
g = acceleration due to gravity, m/s^2
g_0 = Radial-distribution function
h = height of bubble above distribution, cm
I = identity tensor
k = conductivity of particulate fluctuating energy
Nu = Nusselt number
p = pressure, Pa
pr = prandtl number
p_s = solids pressure
Re = Reynolds number
t = clock time, s
V = velocity, m/s
u = fluidization velocity, m/s

Greek letters

β = gas-particle exchange coefficients, kg/m^3 · s
ε = volume fraction
ρ = density, kg/m^3
λ = volume concentration of solids
τ = viscous stress tensor, N^2/m^2
μ = viscosity, kg/m · s
θ = granular temperature, m^2/s^2
ζ = Gas-particle transfer area, m^2

Subscripts

D = particle
g = gas phase
k = turbulence
i, j, k = coordinate direction
s = solids phase

Literature Cited

1. Dyakowski T, Edwards RB, Xie CG, Williams RA. Application of capacitance tomography to gas-solid flows. *Chem Eng Sci.* 1997;52: 2099–2110.
2. Dyakowski T, Luke SP, Ostrowski KL, Williams RA. On-line monitoring of dense phase flow using real time dielectric imaging. *Powder Technol.* 1999;104:287–295.
3. Halow JS, Fasching GE, Nicoletti P, Spenik JL. Observation of fluidized bed using capacitance imaging. *Chem Eng Sci.* 1993;48:643–659.
4. Wang SJ, Dyakowski T, Xie CG, Beck MS, Williams RA. Real time capacitance imaging of bubble formation at the distributor of a fluidized bed. *Chem Eng J and the Biochemical Eng J.* 1995;56:95–100.
5. Makkawi YT, Wright PC. Electrical capacitance tomography for conventional fluidized bed measurements-remarks on the measuring technique. *Powder Technol.* 2004;148:42–157.
6. Liu S, Wang S, Mason DJ, Dyakowski T, Geldart D. Measurement of solids concentration in gas-solid flows using capacitance tomography and pressure sensors. *Sensors and their Application VIII,* eds. AT Augousti and NM White. Institute of Physics Publishing, Bristol and Philadelphia; 1997:101.
7. Du B, Warsito W, Fan LS. ECT studies of gas-solid fluidized beds of difference diameters. *Ind Eng Chem Res.* 2005;44:5020–5030.
8. Yang WQ, Liu S. Electrical capacitance tomography with square sensor. *Electronics Letts.* 1999;35:295–296.
9. Liu S, Yang WQ, Wang H, Jiang F, Su Y. Investigation of square fluidized beds using capacitance tomography: preliminary results. *Meas Sci and Technol.* 2001;12:1120–1125.
10. Liu S, Wang HG, Jiang F, Yang WQ. A new image reconstruction method for tomographic investigation of fluidized beds. *AIChE J.* 2002;48:1631–1638.
11. Liu S, Fu L, Yang WQ. Optimization of an iterative image reconstruction algorithm for electrical capacitance tomography. *Meas Sci and Technol.* 1999;10:L37–L39.
12. Soo SL. *Fluid dynamics of multiphase systems.* New York: Blaisdell Press; 1967.
13. Gidaspow D, Ettehadieh B. Fluidization in two dimensional beds with a jet: Part II. Hydrodynamic modelling. *Int Eng Chem Fundam.* 1983;22:193–201.
14. Ding J, Gidaspow D. A bubbling fluidization model using kinetic theory of granular flow. *AIChE J.* 1990;36:523–538.
15. Gidaspow D, Bezburuah R, Ding J. Hydrodynamics of Circulating fluidized bed, Kinetic theory approach. In Fluidization VII. *Proc. of 7th Eng. Foundation Conference on Fluidization.* Brisbane, Australia; May 3–8;1992:75–82.
16. Lun CKK, Savage SB, Jeffrey DJ, Chepurniy N. Kinetic theories for granular flow: Inelastic particles in couette flow and slightly inelastic particles in a general flow field. *J Fluid Mech.* 1984;140:223–256.
17. Yang WQ, York TA. New AC-based capacitance tomography system. *IEE Proc-Sci Meas Technol.* 1999;146:47–53.
18. Johnson PC, Jackson R. Frictional-collisional constitutive relations for granular materials, with application to plane shearing. *J Fluid Mech.* 1987;176:67–93.
19. Sinclair JL, Jackson R. Gas-particle flow in a vertical pipe with particle-particle interactions. *AIChE J.* 1989;35:1473–1486.
20. Peirano E, Delloume V, Leckner B. Two- or three-dimensional simulations of turbulent gas-solid flows applied to fluidization. *Chem Eng Sci.* 2001;56:4789–4799.
21. Peirano E, Delloume V, Johnsson F, Leckner B, Simonin O. Numerical simulation of the fluid dynamics of a freely bubbling fluidized bed: influence of the air supply system. *Powder Technol.* 2002;122:69–82.
22. Pain CC, Mansoorzadeh S, Oliverira CRE. A study of bubbling and slugging fluidised beds using the two-fluid granular temperature model. *Int J Multiphase Flow.* 2001;27:527–551.
23. Wachem BGM, Schouten JC, Kirshna R, van den Bleek CM. Eulerian simulation of bubbling behaviour in gas-solid fluidised beds. *Computers Chem Eng.* 1998;22:S299–S306.
24. Ergun S. Fluid flow through packed columns. Chemical Engineering Progress. 1952;48:89–94.
25. Clift R, Grace JR. *Continuous bubbling and slugging.* London: Academic Press; 1985.
26. Grace JR, Harrison D. The influence of bubble shape on the rising velocities of large bubble. *Chem Eng Sci.* 1967;22:1337–1347.
27. Darton RC, LaNauze RD, Davidson J, Harrison D. Bubble growth due to coalescence in fluidised beds. *Trans IChemE.* 1977;55:274–280.
28. Svensson A, Johnsson F, Leckner B. Fluidization regimes in nonslugging fluidized bed: Influence of pressure drop across the air distributors. *Powder Technol.* 1996;86:229–312.
29. Zijerveld RC, Johnsson F, Marzocchella A, Schouten J, van den Bleek C. Fluidization regimes and transition from fixed bed to dilute transport flow. *Powder Technol.* 1998;95:185–204.
30. Schouten JC, van den Stappen MLM, van den Bleek CM. *Detterministic chaos analysis of gas-solid fluidization.* In OE Potter and DJ Nicklin, eds. Fluidization VII, New York: Engineering Foundation; 1992.
31. Johnsson F, Zijerveld RC, Schouten JC, van den Bleek CM, Leckner B. Characterization of fluidization regimes by time-series analysis of pressure fluctuations. *Int J Multiphase Flow.* 2000;26:663–715.
32. Pain CC, Mansoorzadeh S, Gomes JLM, de Oliveira CrE. A numerical investigation of bubbling gas solid fluidized bed dynamics in 2-D geometries. *Powder Technol.* 2002;128:56–77.
33. Malcus S, Cruz E, Rowe C, Pugsley TS. Radial solid mass flux profiles in a high-suspension density circulating fluidized bed. *Powder Technol.* 2002;125:5–9.
34. Kuhn FT, Schouthen JC, Mudde RF, van Den Bleek CM, Scarlett B. Analysis of chaos in fluidization using electrical capacitance tomography. *Meas Sci and Technol.* 1996;7:361–368.

Appendix

Constitutive equations of two-fluid models

(a) Gas-particle interphase-drag coefficients

$$\varepsilon_g < 0.8, \quad \beta = 150\,\frac{(\varepsilon_s)^2\mu_g}{\varepsilon_g d_s^2} + 1.75\,\frac{\rho_g\varepsilon_s|\vec{V}_g - \vec{V}_s|}{d_s} \tag{A1}$$

$$\varepsilon_g \geq 0.8, \quad \beta = \frac{3}{4}\,C_d\,\frac{\varepsilon_s\varepsilon_g\rho_g|\vec{V}_g - \vec{V}_s|}{d_s}\,\varepsilon_g^{-2.65} \tag{A2}$$

$$\mathrm{Re}_s = \frac{\varepsilon_s\rho_g|\vec{V}_g - \vec{V}_s|d_s}{\mu_g} < 1000, \quad C_d = \frac{24}{\mathrm{Re}_s}\left[1 + 0.15(\mathrm{Re}_s)^{0.687}\right] \tag{A3}$$

$$\mathrm{Re}_s > 1000, \quad C_d = 0.44 \tag{A4}$$

(b) Gas-phase stress

$$\bar{\bar{\tau}}_g = \mu_g[(\nabla\vec{V}_g + (\nabla\vec{V}_g)^T)] \tag{A5}$$

(c) Solid-phase stress

$$\bar{\tau}_s = -[\xi_s\nabla\cdot\vec{V}_s I + \mu_s(\nabla\vec{V}_s + (\nabla\vec{V}_s)^T] \tag{A6}$$

(d) Dissipation fluctuation energy

$$\gamma_s = 3(1 - e^2)\varepsilon_s^2\rho_s g_0\theta\left(\frac{4}{d}\,\sqrt{\frac{\theta}{\pi}} - \nabla\cdot\vec{V}_s\right) \tag{A7}$$

(e) Radial-distribution function at contact

$$g_0 = \left[1 - \left(\frac{\varepsilon_s}{\varepsilon_{s,\max}}\right)^{1/3}\right]^{-1} \tag{A8}$$

(f) Solid pressure

$$P_s = \varepsilon_s\rho_s\theta[1 + 2g_0\varepsilon_s(1 + e)] \tag{A9}$$

(g) Shear viscosity of solid

$$\mu_s = \frac{4}{5}\,\varepsilon_s^2\rho_s d_s g_0(1 + e)\,\sqrt{\frac{\theta}{\pi}} + \frac{10\rho_s d_s\sqrt{\pi\theta}}{96(1 + e)\varepsilon_s g_0}\left[1 + \frac{4}{5}\,g_0\varepsilon_s(1 + e)\right]^2 \tag{A10}$$

(h) Conductivity of particulate fluctuating energy

$$k_s = \frac{150\rho_s d_s\sqrt{(\theta\pi)}}{384(1 + e)\,g_0}\left[1 + \frac{6}{5}\,\varepsilon_s g_0(1 + e)\right]^2 + 2\rho_s d_s^2(1 + e)\,g_0\sqrt{\frac{\theta}{\pi}} \tag{A11}$$

(i) Bulk solid viscosity

$$\xi_s = \frac{4}{3}\,\varepsilon_s^2\rho_s d g_0(1 + e)\,\sqrt{\frac{\theta}{\pi}} \tag{A12}$$

(j) Exchange of fluctuating energy between gas and particles

$$\phi_s = -3\beta\theta \tag{A13}$$

Table A1. Parameters and Equations Listed in the CFD

Parameter name	Parameter	Number	Equation	Number
Gas velocity	$\vec{V}_g$	3	(1)~(5)	9
Solid velocity	$\vec{V}_s$	3		
Gas pressure	P_g	1		
Volume fraction for gas	ε_g	1		
Volume fraction for solid	ε_s	1		
Granular temperature	θ	1	(7)	1
Gas-particle exchange coefficients	β	1	(A1)	1
Gas stress tensor	$\bar{\tau}_g$	1	(A5)	1
Solid stress tensor	$\bar{\tau}_s$	1	(A6)	1
Dissipation fluctuation energy	γ_s	1	(A7)	1
Radial distribution function at contact	g_0	1	(A8)	1
Solid pressure	P_s	1	(A9)	1
Solid viscosity	μ_s	1	(A10)	1
Conductivity of particulate fluctuating energy	k_s	1	(A11)	1
Bulk solid viscosity	ζ_s	1	(A12)	1
Exchange of fluctuating energy between gas and particles	ϕ_s	1	(A13)	1
Total		20		20

Manuscript received Nov. 29, 2005, and revision received Apr. 20, 2006.